CMS Physics Analysis Summary

Contact: cms-pag-conveners-susy@cern.ch 2015/08/27

Search for Supersymmetry in $H \to \gamma\gamma$ final states with the razor variables at $\sqrt{s} = 8$ TeV

The CMS Collaboration

Abstract

A search for Higgs bosons in decays of supersymmetric particles is presented, using the LHC proton-proton collision data collected by the CMS experiment at a center-of-mass energy $\sqrt{s} = 8$ TeV and corresponding to an integrated luminosity of 19.8 fb^{-1}. Higgs bosons are reconstructed in diphoton final states in association with at least one jet. The razor variables M_R and R^2 are used to categorize events into different regions to improve signal-to-background discrimination. The results are interpreted as constraints on a set of simplified SUSY benchmark models.

1 Introduction

The discovery of the Higgs boson (H) [1–3] at the LHC was achieved through searches designed around its predicted properties in the Standard Model (SM). There are various ways in which new physics can manifest itself in H events. If the H couplings to the known SM particles are modified by new physics, such as effects due to additional loop contributions from new particles , extended Higgs sectors, and Higgs compositeness, the decay modes and branching ratios of the Higgs could deviate from SM predictions. On-shell production of new heavy states can lead to Higgs production processes through cascade decays as discussed in searches for SM-like H's in several models, such as models involving extra Higgs states of the minimal supersymmetric standard model and its extensions, or for composite Higgs models. Conversely the discovery sensitivity for new physics through Higgs production has been studied in the context of supersymmetry with a bino lightest SUSY particle (LSP), a gravitino LSP, and additional weakly coupled LSPs, as well as in the context of vector-like heavy quarks. Higgs production in cascade decays has also been studied as a way to probe the details of the spectra and coupling of new particles after their discovery. In searches for new physics at the LHC, H's produced from the cascade decays of electroweakinos [4–7] and squarks [8] have been considered.

In this paper, we present a search for excess H production [9] interpreted within a class of SUSY models with neutralino next-to-lightest SUSY particles (NLSPs) which dominantly decay to a Higgs boson. The interpretation of the search is given for two such benchmark electroweakino production models with WH and HH final states. Additional benchmark models can be employed to interpret the results in ZH final states and well as models with light third generation squark production. The analysis considers events with one H candidate, reconstructed from a pair of photons, in association with at least one jet. Since a narrow resonance is searched for in the diphoton mass, the backgrounds can be directly determined from the data and the observation of a peak near the H mass would strongly suggest new physics involving production of an on-shell Higgs. The razor variables [10, 11] M_{R} and R^2 are used to discriminate SUSY signatures from the SM backgrounds. All possible combinations of the reconstructed jets and the Higgs candidate are clustered to form megajets [12]. The pair of resulting megajets that minimize the scalar sum of the invariant masses of the two megajets is selected. The razor variables M_{R} and R^2 are computed from the four momenta of the two megajets and the missing transverse momentum $\vec{p}_{\mathrm{T}}^{\,\mathrm{miss}}$:

$$M_{\mathrm{R}} \equiv \sqrt{(|\vec{p}^{\,j_1}| + |\vec{p}^{\,j_2}|)^2 - (p_z^{j_1} + p_z^{j_2})^2}, \tag{1}$$

$$\mathrm{R}^2 \equiv \left(\frac{M_{\mathrm{T}}^{\mathrm{R}}}{M_{\mathrm{R}}}\right)^2, \tag{2}$$

where $\vec{p}$ and p_z are the momentum of a particle and its longitudinal component, respectively, and the labels j_1 and j_2 refer to the two selected megajets. In the definition of R^2, the variable $M_{\mathrm{T}}^{\mathrm{R}}$ is defined as:

$$M_{\mathrm{T}}^{\mathrm{R}} \equiv \sqrt{\frac{E_{\mathrm{T}}^{\mathrm{miss}}(p_{\mathrm{T}}^{j_1} + p_{\mathrm{T}}^{j_2}) - \vec{p}_{\mathrm{T}}^{\,\mathrm{miss}} \cdot (\vec{p}_{\mathrm{T}}^{\,j_1} + \vec{p}_{\mathrm{T}}^{\,j_2})}{2}}. \tag{3}$$

where p_{T} is the transverse momentum and $E_{\mathrm{T}}^{\mathrm{miss}}$ indicates the magnitude of $\vec{p}_{\mathrm{T}}^{\,\mathrm{miss}}$. A search for SUSY in diphoton events also using the razor variables has been performed by CMS [13], without requiring the photon pair to be compatible with the Higgs boson hypothesis.

This paper is organized as follows: in Section 2 the main features of the CMS experimental apparatus are highlighted. In Section 3 the data and simulated samples are described, including a description of the benchmark signal models utilized to interpret the results. The event

selection is discussed in Section 4 while Section 5 describes the breakdown of the selected event sample in independent categories. The background prediction methods are discussed in Section 6. The analysis results and interpretation are shown in Section 7 and Section 8 respectively. A summary is given in Section 9.

2 CMS detector

The central feature of the CMS apparatus is a superconducting solenoid of 6 m internal diameter, providing a magnetic field of 3.8 T. Within the superconducting solenoid volume are a silicon pixel and strip tracker, a lead tungstate crystal electromagnetic calorimeter (ECAL), and a brass/scintillator hadron calorimeter (HCAL), each composed of a barrel and two endcap sections. Muons are measured in gas-ionization detectors embedded in the steel flux-return yoke outside the solenoid. Extensive forward calorimetry complements the coverage provided by the barrel and endcap detectors. A more detailed description of the CMS detector, together with a definition of the coordinate system used and the basic kinematic variables, can be found in Ref. [14].

The energy resolution for photons with $E_{\mathrm{T}} \approx 60\,\mathrm{GeV}$ varies between 1.1% and 2.6% over the solid angle of the ECAL barrel, and from 2.2% to 5% in the endcaps. The HCAL, when combined with the ECAL, measures jets with a resolution $\Delta E/E \approx 100\%/\sqrt{E\,[\mathrm{GeV}]} \oplus 5\%$ [15].

The first level (L1) of the CMS trigger system, composed of custom hardware processors, uses information from the calorimeters and muon detectors to select the most interesting events in a fixed time interval of less than 4 μs. The high level trigger (HLT) processor farm further decreases the event rate from around 100 kHz to around 400 Hz, before data storage.

3 Datasets

The analysis uses data collected by the CMS experiment in 2012. Events used in the analysis are collected by a set of diphoton trigger algorithms implemented for the H discovery [16]. The highest-p_{T} photon is required to have $p_{\mathrm{T}} > 36$ GeV and the next highest p_{T} photon must have $p_{\mathrm{T}} > 22$ GeV. The trigger selection imposes relaxed identification and isolation criteria on the photons achieving a high efficiency for selecting two real photons. The efficiency of the online selection is found to be $(81 \pm 5)\%$ for events selected with the analysis criteria used and is independent of the kinematic properties of the events.

3.1 Background samples

There are two types of background that are relevant for this search: non-resonant backgrounds from QCD processes, and resonant background from Standard Model Higgs production. The main background contribution in the analysis is a mixture of QCD single- and double-photon production in association with jets, as well as dijet production where both jets are mis-identified as photons. We predict the QCD background based on data-driven methods. The PYTHIA V6.4.26 [17] and SHERPA 1.4.0 [18–21] Monte Carlo (MC) event generators are used to simulate data samples of these backgrounds.

The production of the SM Higgs boson in the four leading production modes is summarized in table 1. For this background the H mass is assumed to be $m_H = 125$ GeV and the branching ratio for the diphoton decay is fixed to $Br(H \to \gamma\gamma) = 2.28 \times 10^{-3}$, as predicted by the SM [22]. Gluon-fusion and vector-boson-fusion production modes are simulated with POWHEG [23, 24], and matched to PYTHIA for parton showering. PYTHIA is used to simulate associated WH

and ZH as well as $t\bar{t}H$ production. All simulated samples are processed through a GEANT4-based [25] simulation of the CMS detector.

Table 1: The SM Higgs production mechanisms considered as background to this analysis. The cross-section values correspond to 8 TeV pp collisions with $m_H = 125\,\text{GeV}$ [22].

Process Name	Process	Cross-section (pb)	Expected Events in 19.8 fb^{-1}
Gluon Fusion	$pp \to H$	19.3	870
Vector Boson Fusion	$pp \to qqH$	1.6	71
Associated Production	$pp \to VH$	1.1	51
Top Associated Production	$pp \to ttH$	0.13	5.8
Total		22	998

3.2 Benchmark signal samples

Two SUSY simplified models (SMS) [26–30] are considered for the interpretation of the search results. The first is based on an R-parity-conserving gauge-mediated SUSY-breaking (GMSB) model [31, 32] in which the two lightest neutralinos $\tilde{\chi}_2^0$ and$\tilde{\chi}_1^0$ and the lightest chargino $\tilde{\chi}_1^\pm$ are higgsinos and are approximately mass degenerate. The LSP is the gravitino $\widetilde{G}$ [33], the SUSY partner of the graviton, and its mass is assumed to be 1 GeV. The $\tilde{\chi}_1^0$ higgsino, which is the NLSP, undergoes a two-body decay to either an H boson and $\widetilde{G}$ or to a Z boson and $\widetilde{G}$, where $\widetilde{G}$ is stable, and weakly interacting. The pair production of any of the combinations $\tilde{\chi}_2^0\tilde{\chi}_1^0$ $\tilde{\chi}_2^0\tilde{\chi}_1^\pm$, $\tilde{\chi}_1^0\tilde{\chi}_1^\pm$ or $\tilde{\chi}_1^\pm\tilde{\chi}_1^\pm$ is allowed [31], enhancing the effective production cross section for the $\tilde{\chi}_1^0\tilde{\chi}_1^0$ di-higgsino state and thus for HH and ZH production.

The second example of a SUSY scenario with Higgs bosons considered for interpretation of the search results is the R-parity-conserving chargino-neutralino $\tilde{\chi}_2^0\tilde{\chi}_1^\pm$ electroweak pair production process in which the chargino $\tilde{\chi}_1^\pm$ is wino-like and the $\tilde{\chi}_1^0$ neutralino is a massive, stable, weakly interacting bino-like LSP, where the wino and bino are the SUSY partners of the W and B gauge bosons respectively. This scenario represents the SUSY process with the largest electroweak cross section [34]. It leads to the WH topology, with missing energy present due to the presence of the two LSP's. Only $H \to \gamma\gamma$ decays are considered.

Events are generated with MADGRAPH V5 [35, 36], where the SUSY particles are produced in association with up to two additional partons from initial-state radiation. PYTHIA is used for parton showering and hadronization, as well as for the decay of SUSY particles . The matching between MADGRAPH and PYTHIA is performed according to the MLM algorithm [37]. Events are processed through the full GEANT4-based [25] simulation of the CMS detector. Production cross sections are calculated at the next-to-leading order (NLO) plus next-to-leading-logarithm (NLL) accuracy, using the RESUMMINO calculation [38, 39]. The electroweakino production benchmark models used in this analysis are also used in [40].

4 Event selection

Events are selected with at least one good primary vertex. If more than one vertex is found, the one with the highest p_T^2 sum of associated tracks is chosen as the interaction point for event reconstruction.

Photon candidates are selected with $p_\text{T} > 25$ GeV and $|\eta| < 1.44$, satisfying requirements based on cluster shape and isolation [16]. Photon candidates in the endcap are not considered as they suffer from worse signal-to-background ratio and have worse energy resolution.

Pairs of selected photons are considered as H candidates if at least one of the two photons has $p_{\mathrm{T}} > 40$ GeV and the diphoton mass satisfies $m_{\gamma\gamma} > 100$ GeV. If more than one H candidate is found, the candidate with the highest scalar sum p_{T} of the two photons is selected. The event is rejected if no H candidate with $p_{\mathrm{T}} > 20$ GeV is found. Using simulated events, this selection is proven to minimize the probability of selecting the wrong photon pair in events with a produced H while not biasing the $m_{\gamma\gamma}$ distribution from randomly paired photons.

Jets are reconstructed using a global event description based on the CMS particle flow (PF) algorithm [41, 42]. Individual particles (PF candidates) are reconstructed by combining the information from the inner tracker, the calorimeters, and the muon system. These particles are then clustered into jets, using the FastJet [43] implementation of the anti-k_{T} [44] algorithm with the distance parameter $R = 0.5$. Events with at least one jet with $p_{\mathrm{T}} > 30$ GeV and pseudorapidity $|\eta| < 3.0$ are considered. The jet is required not to overlap with the two photons from the H candidate, imposing a separation $\Delta R = \sqrt{(\Delta\eta)^2 + (\Delta\phi)^2} > 0.5$. The vectorial sum of the reconstructed p_{T} of the PF particles is used to quantify the $\vec{p}_{\mathrm{T}}^{\,\mathrm{miss}}$ in the event. Events with detector- and beam-related noise that can mimic event topologies with high energy and large $E_{\mathrm{T}}^{\mathrm{miss}}$ are filtered using dedicated noise reduction algorithms [45–47].

The combined secondary vertex (CSV) tagging algorithm [48] is used to identify jets originating from the showering and hadronization of b quarks. Jet pairs are identified as $\mathrm{b\bar{b}}$ candidates if both jets satisfy the loose requirement that the CSV discriminator be larger than 0.244, and one of the jets also satisfies the medium requirement that the CSV discriminator be larger than 0.679. Among all the jet pairs selected by these criteria, the pair with mass closest to 125 GeV or 91.2 GeV is chosen as the $H \to \mathrm{b\bar{b}}$ or $Z \to \mathrm{b\bar{b}}$ candidate, respectively. This information is used in Sec. 5 to classify the events in disjoint signal region event categories.

5 Search Region Categories

Selected events are divided into the following categories: the `HighPt` category contains all the events with $p_T^{\gamma\gamma} > 110$ GeV; the `Hbb` category, comprises the remaining events with a $H \to \mathrm{b\bar{b}}$ candidate with mass $110 \leq m_{\mathrm{b\bar{b}}} \leq 140$ GeV; the `Zbb` category, includes the remaining events with a $Z \to \mathrm{b\bar{b}}$ candidate with mass $76 \leq m_{\mathrm{b\bar{b}}} \leq 106$ GeV; the `HighRes` category, contains all the other events with both photons satisfying $\sigma_E/E < 0.015$, where σ_E/E is the relative energy resolution for the identified photons. Finally the `LowRes` category is composed of the remaining events. A schematic showing the hierarchy of the event categories is presented in Fig. 1. The motivation for the first three categories is based on the kinematics of the considered SMSs. For events where there is a large mass splitting between the pair-produced particle and the LSP, the H is produced with large momentum, and hence preferentially populates the `HighPt` category. We expect this category to have low background, as combinatorial QCD backgrounds are less likely to produce a di-photon pair that is both high mass and highly boosted. For cases where a second H is produced, the majority of such events contain a $b\bar{b}$ pair peaking at the H mass. Similarly, if a Z boson is produced, a $b\bar{b}$ pair near the Z mass can be observed. The final two categories are used to capture signal events in a less model-dependent way. By selecting high resolution photons in the `HighRes` category we suppress the contamination of hadrons misidentified as photons, which typically have wide clusters and thus worse resolutions, and enhance the best measured real photons. To avoid bias from the observed data, these selection criteria were established without considering data in the signal regions [49, 50].

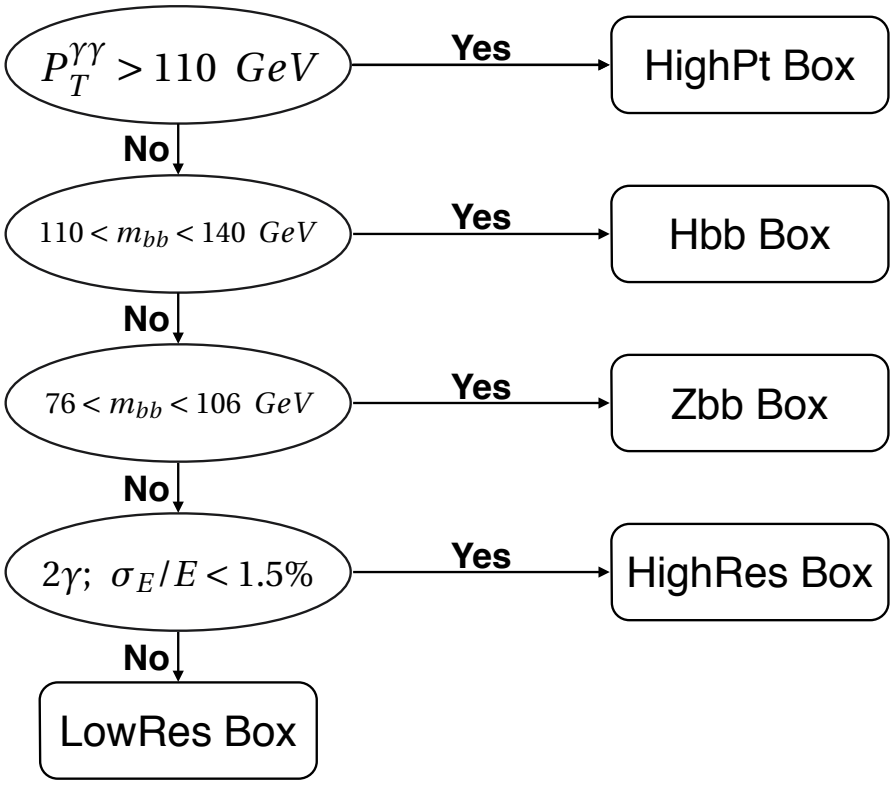

Figure 1: Hierarchy of event categories.

6 Background prediction

Two classes of background events also pass the selection criteria described in Sec. 4: the Standard Model Higgs background, represented by events with a Higgs boson decaying to two photons in the final state, and a combinatorial background dominated by QCD processes, in which two real or fake photons are combined to form a Higgs boson candidate. The Standard Model Higgs background is estimated from the Monte Carlo simulation, while the combinatorial background is predicted from a data control sample.

In each category, the events are divided into the Higgs search region and the upper and lower sidebands, based on the value of $m_{\gamma\gamma}$. The search region is defined according to σ_{eff}, a measure of the diphoton mass resolution. σ_{eff} is defined such that 68.2% of Higgs boson events fall in an interval of $\pm\sigma_{eff}$ around the nominal m_H value. An estimate of σ_{eff} is derived from simulated events. The σ_{eff} is 1.46 GeV in the `HighRes` category, 2.50 GeV in the `LowRes` category, and 1.56 GeV in the `HighPt` category. For the `Hbb` and `Zbb` categories, the simulation sample is not sufficiently large to obtain an accurate estimate, and therefore we use the overall average value of 2 GeV for σ_{eff}. In order to accomodate the uncertainty in the Higgs mass and to absorb potentially larger tails in the $m_{\gamma\gamma}$ distribution, we define the search region as the interval $(125 - 2\sigma_{eff}, 126 + 2\sigma_{eff})$ in each event category.

The combinatorial background in the (M_{R},R^2) plane in the search region around the m_H peak is estimated using a data-driven technique based on the observed yields in the upper and lower $m_{\gamma\gamma}$ sidebands, defined as $131 < m_{\gamma\gamma} < 160$ GeV and $103 < m_{\gamma\gamma} < 120$ GeV, respectively. We observe from the Monte Carlo simulation as well as a data control sample enriched in multijet events that the shape of the $m_{\gamma\gamma}$ distribution is independent of M_{R} and R^2. Therefore, we fit the $m_{\gamma\gamma}$ sideband distribution in each category using the sum of two independent exponential functions, inclusive in M_{R} and R^2, to obtain a model for the $m_{\gamma\gamma}$ shape. Based on this shape

model, we obtain transfer factors that predict the background yield in the search region given the observed yield in the sideband region. Alternative fit functions are considered and the differences in the predicted shapes are used to define a systematic uncertainty. The transfer factors, defined as the ratio of the integral of the best-fit function over the search region to the integral of the best-fit function over the sideband regions, for the various event categories are summarized in Table 2.

Table 2: Transfer factors derived from the fits to the $m_{\gamma\gamma}$ upper and lower sideband. The quoted uncertainties account for the statistical uncertainty in the fit and the choice of the functional form. An additional systematic uncertainty accounting for shape uncertainty is included when the transfer factors are used to predict the background, and is described in greater detail in Section 6.1.

Event Category	Background Prediction Transfer Factor
HighPt	0.162 ± 0.004
Hbb	0.212 ± 0.049
Zbb	0.204 ± 0.032
HighRes	0.162 ± 0.002
LowRes	0.259 ± 0.002

In order to reduce the background contamination, $M_R > 150$ GeV is required in each event category. The selected portion of the (M_R,R^2) plane is binned, and the background in each bin is predicted as follows: the combinatorial background is predicted measuring the $m_{\gamma\gamma}$ sideband yield in the same (M_R,R^2) bin and multiplying it by the corresponding transfer factor from Table 2; the Standard Model Higgs background is predicted from simulated events, normalized to an integrated luminosity of 19.8 fb^{-1}. Table 3 shows the expected event yields in each event category, integrated over the (M_R,R^2) bins for the baseline selection with $M_R > 150$ GeV. For completeness, Table 4 provides the corresponding values for the benchmark signal models and the total uncertainty. The background estimate uncertainty is dominated by the limited event yield in the $m_{\gamma\gamma}$ sideband and the background shape uncertainty, described in greater detail in Section 6.1. The signal uncertainty is dominated by the size of the simulated benchmark samples and the theoretical uncertainty on the signal production cross section.

Table 3: Event yields for the QCD combinatorial, the SM Higgs, and the total background in each event category for the baseline selection with $M_R > 150$ GeV, are shown along with the event yields observed in data.

Event Category	Combinatorial background	SM Higgs background	Total background	Observed Data
HighPt	353 ± 41	20 ± 2	373 ± 41	377
Hbb	4.9 ± 4.0	0.12 ± 0.02	5.0 ± 4.0	1
Zbb	6.7 ± 4.4	0.11 ± 0.04	6.9 ± 4.4	3
HighRes	833 ± 82	33 ± 3	866 ± 82	909
LowRes	1630 ± 109	13 ± 1	1643 ± 109	1640

6.1 Systematic uncertainties

The systematic uncertainties fall into three broad categories: those affecting the normalization of the signal and background Monte Carlo simulation, those affecting the object selection in the simulation, and those describing the uncertainty on the background prediction. Each systematic uncertainty is evaluated separately for each region of the (M_R,R^2) plane in each event

Table 4: Event yields and efficiency ϵ for the two signal benchmark models and for the baseline selection with $M_R > 150$ GeV.

Event Category	$\tilde{\chi}_1^0\tilde{\chi}_1^0$ production				$\tilde{\chi}_2^0\tilde{\chi}_1^\pm$ production			
	$m_{\tilde{\chi}_1^0} = 130$ GeV		$m_{\tilde{\chi}_1^0} = 175$ GeV		$m_{\tilde{\chi}_2^0} = 130$ GeV		$m_{\tilde{\chi}_2^0} = 175$ GeV	
	ϵ (%)	Yield	ϵ (%)	Yield	ϵ (%)	Yield	ϵ (%)	Yield
HighPt	$8.6^{+0.5}_{-0.5}$	$12.6^{+0.7}_{-0.7}$	$11.1^{+0.6}_{-0.6}$	$5.1^{+0.3}_{-0.3}$	$8.9^{+0.6}_{-0.6}$	$16.6^{+1.0}_{-1.0}$	$10.7^{+0.5}_{-0.5}$	$6.4^{+0.3}_{-0.3}$
Hbb	$1.8^{+0.1}_{-0.1}$	$2.6^{+0.2}_{-0.2}$	$1.8^{+0.1}_{-0.1}$	$0.8^{+0.1}_{-0.1}$	—	—	—	—
Zbb	$0.6^{+0.0}_{-0.1}$	$0.9^{+0.1}_{-0.1}$	$0.7^{+0.1}_{-0.1}$	$0.3^{+0.0}_{-0.0}$	—	—	—	—
HighRes	$4.7^{+0.2}_{-0.2}$	$6.9^{+0.3}_{-0.4}$	$5.3^{+0.3}_{-0.3}$	$2.5^{+0.1}_{-0.1}$	$5.2^{+0.3}_{-0.3}$	$9.7^{+0.6}_{-0.6}$	$6.5^{+0.3}_{-0.3}$	$3.9^{+0.2}_{-0.2}$
LowRes	$1.9^{+0.1}_{-0.1}$	$2.8^{+0.1}_{-0.2}$	$2.2^{+0.1}_{-0.1}$	$1.0^{+0.1}_{-0.1}$	$2.2^{+0.1}_{-0.1}$	$4.1^{+0.3}_{-0.3}$	$2.6^{+0.1}_{-0.1}$	$1.6^{+0.1}_{-0.1}$

category. The individual sources of background systematic uncertainty are assumed to be uncorrelated.

The simulation normalization systematic uncertainties are listed in Table 5. The luminosity systematic uncertainty is the measurement uncertainty of the delivered luminosity, which affects the normalization of the Monte Carlo simulation predictions and is assumed to be fully correlated across all event categories. The simulation is normalized to take into account the total trigger efficiency and so the uncertainty is added as a systematic uncertainty on this normalization.

The theory uncertainties on the Standard Model Higgs background are per-process uncertainties on the production cross-section taken from [22]. These uncertainties arise from higher-order electroweak and QCD radiative corrections and uncertainties on the parton distribution functions (PDF's). The SMS signal theory uncertainties affect the normalization of the benchmark signal models. They are described in [51] and reflect similar normalization uncertainties.

Systematic uncertainties related to object reconstruction performance in the Monte Carlo simulation are also summarized in Table 5. These systematic effects are treated by varying the nuisance parameter corresponding to each effect up and down by the size of the corresponding uncertainty and re-computing the expected Standard Model Higgs background yields. The difference with respect to the nominal values is taken as the $\pm 1\sigma$ size of the resultant uncertainty. Apart from the b-tagging uncertainty, these systematic uncertainties affect the selection efficiency and the normalization. The b-tagging systematic is measured as the difference in the efficiency to tag b quarks in data versus that in corrected MC in the analysis. This correction is done by weighting events based on the number and p_T of the b-tagged jets versus non-btagged jets in the event, and the uncertainty on this correction is taken as a systematic. The size of the uncertainty varies as a function of the number and p_T of the jets in the event, and is computed event-by-event.

The final set of systematic uncertainties are those that arise from limited size of the Monte Carlo simulation samples as well as the sideband regions, and are summarized in table 5. These are by far the largest systematic uncertainties and the only ones that affect the sideband prediction. A shape uncertainty on the data-driven QCD background prediction is included, which reflects a possible variation in the shape of the $m_{\gamma\gamma}$ distribution across the different bins in the (M_R, R^2) plane. Based on sideband fits to the data, we obtain separate transfer factors that predict the non-resonant background yield in the search regions based on the upper or lower sidebands alone. The difference between these predictions and the nominal prediction is taken as the systematic uncertainty on the background shape.

Table 5: Systematic uncertainties.

MC normalization systematic uncertainties		
Source	value	target
luminosity	2.5%	Signal Models, SM Higgs boson MC
trigger efficiency	5%	Signal Models, SM Higgs boson MC
Higgs boson theory	$2\% - 8\%$	SM Higgs boson MC
signal theory x-sec uncertainty	$\approx 13\%$	
Object-level systematic uncertainties		
jet energy scale	shape (3%)	Signal Models, SM Higgs boson MC
photon energy and resolution	shape (1%)	Signal Models, SM Higgs boson MC
b-tagging ID	shape $(0 - 4\%)$	Signal Models, SM Higgs boson MC
σ_E / E uncertainty	shape	Signal Models, SM Higgs boson MC
Normalization & shape systematic uncertainties		
background prediction uncertainty	$1\% - 50\%$	background shape
sideband yields	$1 - 100\%$	low event yields in the data sidebands
fit choice	$\approx 1\%$	background normalization
MC statistics	varies	statistics in SM Higgs boson and SMS MC

7 Results

The background predictions are compared to the observed yields in order to test for the presence of a signal. Figure 2 shows the $m_{\gamma\gamma}$ distributions in the five event categories. The fits over the entire (M_R, R^2) plane describe the observed data without any significant deviations.

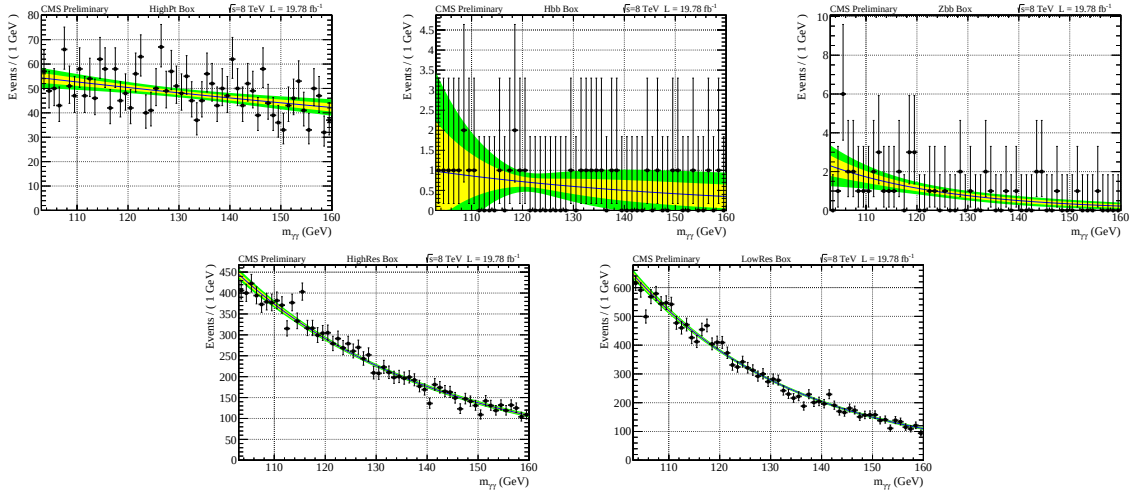

Figure 2: The fits to the $m_{\gamma\gamma}$ distribution in the `HighPt` (top left), `Hbb` (top middle), `Zbb` (top right), `HighRes` (bottom left), and `LowRes` (bottom right) categories integrated over the entire (M_R,R^2) plane. The fits are shown with their $\pm 1\sigma$ (yellow) and $\pm 2\sigma$ (green) uncertainty bands.

Tables 6-10 show the observed event yield in each of the defined (M_R, R^2) bins, as well as the expected yield from the predicted backgrounds and their systematic uncertainties. The p-value of the observation compared to the expectation and the associated significance are also quoted. The p-value is computed using pseudo-experiments by sampling the predicted background for each pseudo-experiment from the sum of independent Gaussian functions for each systematic

Table 6: Number of Events observed in the signal region compared to expected background in the HighPt category.

M_R region	R^2 region	observed events	expected background	p-value	significance (σ)
150 - 200	0.00 - 0.05	4	$3.2^{+1.3}_{-0.9}$(syst.)	0.31	0.5
150 - 200	0.05 - 0.10	3	$3.3^{+0.9}_{-0.7}$(syst.)	0.45	-0.1
150 - 200	0.10 - 0.15	1	$0.8^{+0.5}_{-0.3}$(syst.)	0.41	0.2
150 - 200	0.15 - 0.20	0	$0.2^{+0.2}_{-0.1}$(syst.)	0.50	0.0
150 - 200	0.20 - 1.00	0	$0.3^{+0.3}_{-0.1}$(syst.)	0.50	0.0
200 - 300	0.00 - 0.05	89	$69.7^{+5.1}_{-4.7}$(syst.)	0.028	1.9
200 - 300	0.05 - 0.10	42	$33.0^{+3.5}_{-3.1}$(syst.)	0.095	1.3
200 - 300	0.10 - 0.15	8	$6.4^{+1.6}_{-1.3}$(syst.)	0.28	0.6
200 - 300	0.15 - 1.00	1	$1.3^{+0.7}_{-0.5}$(syst.)	0.44	-0.1
300 - 500	0.00 - 0.05	119	$136.2^{+7.3}_{-6.9}$(syst.)	0.099	-1.3
300 - 500	0.05 - 0.10	21	$20.1^{+2.1}_{-1.9}$(syst.)	0.42	0.2
300 - 500	0.10 - 1.00	3	$2.5^{+0.7}_{-0.6}$(syst.)	0.39	0.3
500 - 1600	0.00 - 0.05	84	$91.8^{+5.7}_{-5.4}$(syst.)	0.24	-0.7
500 - 1600	0.05 - 1.00	0	$1.5^{+0.6}_{-0.4}$(syst.)	0.25	-0.7
1600 - 3000	0.00 - 1.00	2	$2.5^{+0.9}_{-0.7}$(syst.)	0.42	-0.2

Table 7: Number of Events observed in the signal region compared to expected background in the Hbb category.

M_R region	R^2 region	observed events	expected background	p-value	significance (σ)
150 - 300	0.00 - 0.05	0	$1.9^{+1.2}_{-0.7}$(syst.)	0.22	-0.8
150 - 300	0.05 - 1.00	0	$1.3^{+0.7}_{-0.5}$(syst.)	0.32	-0.5
300 - 3000	0.00 - 1.00	1	$1.8^{+1.1}_{-0.7}$(syst.)	0.33	-0.4

effect and generating yields from Poisson functions with expectation values set equal to the Gaussian-samples values.

We observe no significant deviation between observation and expectation in all but one bin in the HighRes category. In the bin 400 GeV $< M_R <$ 1400 GeV $0.05 < R^2 < 1.00$ in the HighRes category, we observe 5 events in the $m_{\gamma\gamma}$ signal region and predict $0.5^{+0.4}_{-0.2}$, which corresponds to a local significance of 2.9σ. Taking into account the possibility that the background fluctuates this high in any of the 46 analysis bins, the corresponding global significance of 1.6σ. An alternative version of the analysis was also considered where simple cuts in the (M_R-R^2) plane were used to avoid the presence of multiple signal regions thus reducing the look elsewhere effect. The significance of the deviation is confirmed with this approach.

Table 8: Number of Events observed in the signal region compared to expected background in the Zbb category.

M_R region	R^2 region	observed events	expected background	p-value	significance (σ)
150 - 450	0.00 - 0.05	1	$2.0^{+1.0}_{-0.7}$	0.44	-0.2
150 - 450	0.05 - 1.00	1	$0.8^{+0.6}_{-0.4}$	0.42	0.2
450 - 3000	0.00 - 1.00	1	$4.0^{+1.6}_{-1.1}$	0.15	-1.1

Table 9: Number of Events observed in the signal region compared to expected background in the HighRes category.

M_R region	R^2 region	observed events	expected background	p-value	significance (σ)
150 - 250	0.00 - 0.05	363	$357.6^{+9.6}_{-9.4}$(syst.)	0.40	0.3
150 - 250	0.05 - 0.10	149	$139.4^{+5.6}_{-5.4}$(syst.)	0.23	0.7
150 - 250	0.10 - 0.15	35	$32.5^{+3.4}_{-3.1}$(syst.)	0.34	0.4
150 - 250	0.15 - 1.00	7	$8.0^{+1.7}_{-1.4}$(syst.)	0.40	-0.3
250 - 400	0.00 - 0.05	218	$207.9^{+7.0}_{-6.8}$(syst.)	0.27	0.6
250 - 400	0.05 - 0.10	20	$14.7^{+2.5}_{-2.1}$(syst.)	0.13	1.1
250 - 400	0.10 - 1.00	3	$2.7^{+0.8}_{-0.6}$(syst.)	0.43	0.2
400 - 1400	0.00 - 0.05	109	$101.6^{+5.0}_{-4.8}$(syst.)	0.26	0.7
400 - 1400	0.05 - 1.00	5	$0.5^{+0.4}_{-0.2}$(syst.)	0.002	2.9
1400 - 3000	0.00 - 1.00	0	$0.9^{+0.5}_{-0.3}$(syst.)	0.44	-0.1

Table 10: Number of Events observed in the signal region compared to expected background in the LowRes category.

M_R region	R^2 region	observed events	expected background	p-value	significance (σ)
150 - 200	0.00 - 0.05	407	$386.2^{+19.8}_{-18.8}$(syst.)	0.22	0.8
150 - 200	0.05 - 0.10	201	$195.4^{+10.4}_{-9.9}$(syst.)	0.37	0.3
150 - 200	0.10 - 0.15	54	$47.8^{+3.9}_{-3.7}$(syst.)	0.22	0.8
150 - 200	0.15 - 0.20	13	$8.6^{+1.9}_{-1.6}$(syst.)	0.12	1.2
150 - 200	0.20 - 1.00	5	$5.2^{+1.4}_{-1.2}$(syst.)	0.48	0.0
200 - 250	0.00 - 0.05	297	$291.8^{+10.1}_{-9.8}$(syst.)	0.40	0.3
200 - 250	0.05 - 0.10	78	$71.6^{+5.8}_{-5.4}$(syst.)	0.26	0.6
200 - 250	0.10 - 0.15	7	$10.2^{+1.9}_{-1.7}$(syst.)	0.18	-0.9
200 - 250	0.15 - 1.00	1	$2.6^{+1.3}_{-0.9}$(syst.)	0.34	-0.4
250 - 400	0.00 - 0.05	386	$400.0^{+15.0}_{-14.5}$(syst.)	0.29	-0.6
250 - 400	0.05 - 0.10	21	$29.2^{+4.2}_{-3.7}$(syst.)	0.10	-1.3
250 - 400	0.10 - 1.00	4	$3.4^{+2.0}_{-1.1}$(syst.)	0.30	0.5
400 - 1200	0.00 - 0.05	159	$185.3^{+10.1}_{-9.6}$(syst.)	0.054	-1.6
400 - 1200	0.05 - 1.00	4	$2.1^{+0.9}_{-0.7}$(syst.)	0.15	1.0
1200 - 3000	0.00 - 1.00	3	$4.0^{+1.6}_{-1.1}$(syst.)	0.37	-0.3

8 Interpretation

Using the yields and uncertainties shown in Tables 6-10, we proceed to set limits on the production cross-sections of the SMS considered in the analysis. Since the distributions in the (M_R,R^2) plane for each signal model depend on the mass spectrum of the neutralino, we set these limits as a function of the mass of the produced neutralino. In the asymmetric case the mass of the chargino is set to be equal to the mass of the neutralino.

The branching ratios are assumed to be $\mathcal{B}(\chi_2 \to H\chi_0) = 100\%$ and $\mathcal{B}(\chi_1^\pm \to W^\pm\chi_0) = 100\%$. In the case of $\chi_2\chi_1^\pm$ production (left in Figure 3) cross sections between 1.5 and 3.0 pb are excluded in the range $130 \leq m_{\chi_2} = m_{\chi_1^\pm} \leq 200$ GeV. For the case of symmetric $\chi_2\chi_2$ production in the HH final state cross sections between 1.7 and 3.9 pb are excluded in the range $130 \leq m_{\chi_2} \leq 200$ GeV.

Figure 4 shows the observed and expected limit divided by the theoretical cross section at each mass. For the models with $\chi_2\chi_1^\pm \to HW^\pm\chi_0\chi_0$ and $\chi_1\chi_1 \to HH\widetilde{G}\widetilde{G}$, the 95% confidence level cross section upper limit are within twice the theory cross-section for the entire mass range

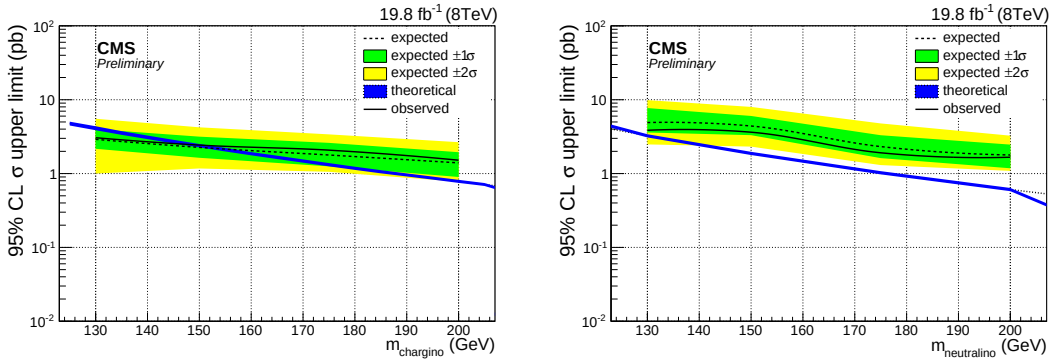

Figure 3: The observed cross-section upper limit for the $\chi_2\chi_1^{\pm} \to HW^{\pm}\chi_0\chi_0$ (left) and $\chi_1\chi_1 \to HH\widetilde{G}\widetilde{G}$ (right) SMSs as a function of the mass of the neutralino (set equal to the mass of the chargino in the left plot) with the mass of the LSP set $m_{LSP} = 1$ GeV. The expected limit, is shown as a dashed line, while the observed limit from the observed data is shown as the solid line. The expected theoretical cross section is shown as the dotted line with the theory uncertainty in blue.

$130 \leq m_{\chi_2} = m_{\chi_1^{\pm}} \leq 200$ GeV. We are able to exclude models with $\chi_2\chi_1^{\pm} \to HW^{\pm}\chi_0\chi_0$ for $m_{\chi_2} = m_{\chi_1^{\pm}} < 150$ GeV.

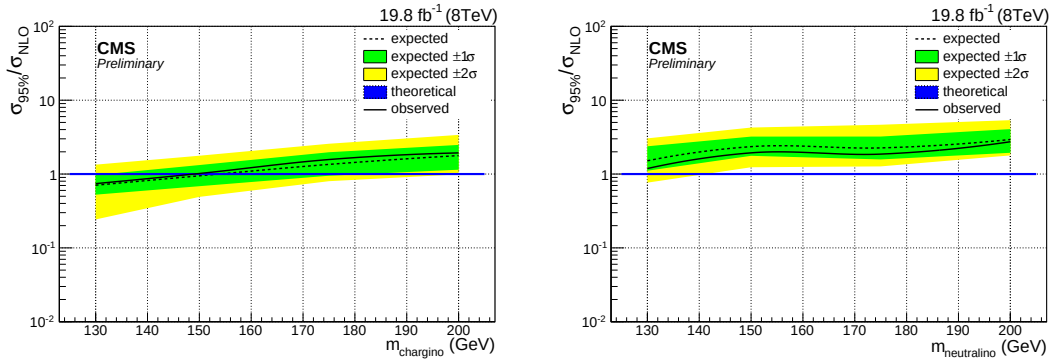

Figure 4: The ratio of the observed cross-section upper limit for the $\chi_2\chi_1^{\pm} \to HW^{\pm}\chi_0\chi_0$ (left) and $\chi_1\chi_1 \to HH\widetilde{G}\widetilde{G}$ (right) SMSs to the theoretical cross section is shown as a function of the mass of the neutralino (set equal to the mass of the chargino in the left) with the mass of the LSP set $m_{LSP} = 1$ GeV. The theory uncertainty is added in quadrature to the experimental uncertainty, though the experimental uncertainty dominates everywhere.

9 Summary

A search for Higgs bosons in decays of supersymmetic particles is performed on the data collected by the CMS experiment at the CERN LHC. Proton collisions collected at a center-of-mass energy $\sqrt{s} = 8$ TeV are considered, corresponding to an integrated luminosity of about $19.8\,\text{fb}^{-1}$. Higgs boson candidates are reconstructed from pairs of photons in the central part of the detector. The razor variables M_R and R^2 are used to suppress the SM Higgs boson production and other SM processes. The majority of the background originates from random pairs of reconstructed photons. The background is constrained using the sidebands of the diphoton mass distribution. The background prediction is found to be compatible with the data observations in the signal search regions and the results are interpreted in terms of models beyond the SM, in which Higgs bosons are produced from the decay of new heavy states. Simplified

models of charginos and neutralinos in SUSY with final states that include WH are excluded for chargino $\chi_1^{\pm}$ masses below 150 GeV.

Acknowledgments

We congratulate our colleagues in the CERN accelerator departments for the excellent performance of the LHC and thank the technical and administrative staffs at CERN and at other CMS institutes for their contributions to the success of the CMS effort. In addition, we gratefully acknowledge the computing centres and personnel of the Worldwide LHC Computing Grid for delivering so effectively the computing infrastructure essential to our analyses. Finally, we acknowledge the enduring support for the construction and operation of the LHC and the CMS detector provided by the following funding agencies: the Austrian Federal Ministry of Science, Research and Economy and the Austrian Science Fund; the Belgian Fonds de la Recherche Scientifique, and Fonds voor Wetenschappelijk Onderzoek; the Brazilian Funding Agencies (CNPq, CAPES, FAPERJ, and FAPESP); the Bulgarian Ministry of Education and Science; CERN; the Chinese Academy of Sciences, Ministry of Science and Technology, and National Natural Science Foundation of China; the Colombian Funding Agency (COLCIENCIAS); the Croatian Ministry of Science, Education and Sport, and the Croatian Science Foundation; the Research Promotion Foundation, Cyprus; the Ministry of Education and Research, Estonian Research Council via IUT23-4 and IUT23-6 and European Regional Development Fund, Estonia; the Academy of Finland, Finnish Ministry of Education and Culture, and Helsinki Institute of Physics; the Institut National de Physique Nucléaire et de Physique des Particules / CNRS, and Commissariat à l'Énergie Atomique et aux Énergies Alternatives / CEA, France; the Bundesministerium für Bildung und Forschung, Deutsche Forschungsgemeinschaft, and Helmholtz-Gemeinschaft Deutscher Forschungszentren, Germany; the General Secretariat for Research and Technology, Greece; the National Scientific Research Foundation, and National Innovation Office, Hungary; the Department of Atomic Energy and the Department of Science and Technology, India; the Institute for Studies in Theoretical Physics and Mathematics, Iran; the Science Foundation, Ireland; the Istituto Nazionale di Fisica Nucleare, Italy; the Ministry of Science, ICT and Future Planning, and National Research Foundation (NRF), Republic of Korea; the Lithuanian Academy of Sciences; the Ministry of Education, and University of Malaya (Malaysia); the Mexican Funding Agencies (CINVESTAV, CONACYT, SEP, and UASLP-FAI); the Ministry of Business, Innovation and Employment, New Zealand; the Pakistan Atomic Energy Commission; the Ministry of Science and Higher Education and the National Science Centre, Poland; the Fundação para a Ciência e a Tecnologia, Portugal; JINR, Dubna; the Ministry of Education and Science of the Russian Federation, the Federal Agency of Atomic Energy of the Russian Federation, Russian Academy of Sciences, and the Russian Foundation for Basic Research; the Ministry of Education, Science and Technological Development of Serbia; the Secretaría de Estado de Investigación, Desarrollo e Innovación and Programa Consolider-Ingenio 2010, Spain; the Swiss Funding Agencies (ETH Board, ETH Zurich, PSI, SNF, UniZH, Canton Zurich, and SER); the Ministry of Science and Technology, Taipei; the Thailand Center of Excellence in Physics, the Institute for the Promotion of Teaching Science and Technology of Thailand, Special Task Force for Activating Research and the National Science and Technology Development Agency of Thailand; the Scientific and Technical Research Council of Turkey, and Turkish Atomic Energy Authority; the National Academy of Sciences of Ukraine, and State Fund for Fundamental Researches, Ukraine; the Science and Technology Facilities Council, UK; the US Department of Energy, and the US National Science Foundation.

Individuals have received support from the Marie-Curie programme and the European Research Council and EPLANET (European Union); the Leventis Foundation; the A. P. Sloan

Foundation; the Alexander von Humboldt Foundation; the Belgian Federal Science Policy Office; the Fonds pour la Formation à la Recherche dans l'Industrie et dans l'Agriculture (FRIA-Belgium); the Agentschap voor Innovatie door Wetenschap en Technologie (IWT-Belgium); the Ministry of Education, Youth and Sports (MEYS) of the Czech Republic; the Council of Science and Industrial Research, India; the HOMING PLUS programme of Foundation for Polish Science, cofinanced from European Union, Regional Development Fund; the Compagnia di San Paolo (Torino); the Consorzio per la Fisica (Trieste); MIUR project 20108T4XTM (Italy); the Thalis and Aristeia programmes cofinanced by EU-ESF and the Greek NSRF; and the National Priorities Research Program by Qatar National Research Fund.

References

[1] ATLAS Collaboration, "Observation of a new particle in the search for the Standard Model Higgs boson with the ATLAS detector at the LHC", *Phys. Lett. B* **716** (2012) 1, doi:10.1016/j.physletb.2012.08.020, arXiv:1207.7214.

[2] CMS Collaboration, "Observation of a new boson at a mass of 125 GeV with the CMS experiment at the LHC", *Phys. Lett. B* **716** (2012) 30, doi:10.1016/j.physletb.2012.08.021, arXiv:1207.7235.

[3] CMS Collaboration, "Observation of a new boson with mass near 125 GeV in pp collisions at $\sqrt{s}$ = 7 and 8 TeV", *JHEP* **06** (2013) 081, doi:10.1007/JHEP06(2013)081, arXiv:1303.4571.

[4] CMS Collaboration, "Searches for electroweak neutralino and chargino production in channels with Higgs, Z, and W bosons in pp collisions at 8 TeV", *Phys. Rev. D* **90** (2014) 092007, doi:10.1103/PhysRevD.90.092007, arXiv:1409.3168.

[5] CMS Collaboration, "Searches for electroweak production of charginos, neutralinos, and sleptons decaying to leptons and W, Z, and Higgs bosons in pp collisions at 8 TeV", *Eur. Phys. J. C* **74** (2014) 3036, doi:10.1140/epjc/s10052-014-3036-7, arXiv:1405.7570.

[6] CMS Collaboration, "Search for top squark and higgsino production using diphoton Higgs boson decays", *Phys. Rev. Lett.* **112** (2014) 161802, doi:10.1103/PhysRevLett.112.161802, arXiv:1312.3310.

[7] ATLAS Collaboration, "Search for direct pair production of a chargino and a neutralino decaying to the 125 GeV Higgs boson in $\sqrt{s} = 8$ TeV pp collisions with the ATLAS detector", *Eur. Phys. J. C* **75** (2015) 208, doi:10.1140/epjc/s10052-015-3408-7, arXiv:1501.07110.

[8] CMS Collaboration, "Search for top-squark pairs decaying into Higgs or Z bosons in pp collisions at $\sqrt{s}$=8 TeV", *Phys. Lett. B* **736** (2014) 371, doi:10.1016/j.physletb.2014.07.053, arXiv:1405.3886.

[9] A. R. Mott, "Search for Higgs Boson Production Beyond the Standard Model Using the Razor Kinematic Variables in pp Collisions at $\sqrt{s}$=8 TeV and Optimization of Higgs Boson Identification Using a Quantum Annealer.". PhD thesis, California Institute of Technology, 2015.

[10] CMS Collaboration, "Inclusive search for squarks and gluinos in pp collisions at $\sqrt{s} = 7$ TeV", *Phys. Rev. D* **85** (2012) 012004, doi:10.1103/PhysRevD.85.012004, arXiv:1107.1279.

[11] C. Rogan, "Kinematics for new dynamics at the LHC", (2010). arXiv:1006.2727.

[12] CMS Collaboration, "Search for supersymmetry with razor variables in pp collisions at $\sqrt{s} = 7$ TeV", *Phys. Rev. D* **90** (2014) 112001, doi:10.1103/PhysRevD.90.112001, arXiv:1405.3961.

[13] CMS Collaboration, "Search for supersymmetry in two-photons+jet events with razor variables in pp collisions at sqrt(s) = 8 TeV", CMS Physics Analysis Summary CMS-PAS-SUS-14-008, 2014.

[14] CMS Collaboration, "The CMS experiment at the CERN LHC", *JINST* **3** (2008) S08004, doi:10.1088/1748-0221/3/08/S08004.

[15] CMS Collaboration, "Energy calibration and resolution of the CMS electromagnetic calorimeter in pp collisions at $\sqrt{s} = 7$ TeV", *JINST* **8** (2013) P09009, doi:10.1088/1748-0221/8/09/P09009, arXiv:1306.2016.

[16] CMS Collaboration, "Observation of the diphoton decay of the Higgs boson and measurement of its properties", *Eur. Phys. J. C* **74** (2014) 3076, doi:10.1140/epjc/s10052-014-3076-z, arXiv:1407.0558.

[17] T. Sjöstrand, S. Mrenna, and P. Skands, "PYTHIA 6.4 physics and manual", *JHEP* **05** (2006) 026, doi:10.1088/1126-6708/2006/05/026, arXiv:hep-ph/0603175.

[18] T. Gleisberg and S. Hoeche, "Comix, a new matrix element generator", *JHEP* **12** (2008) 039, doi:10.1088/1126-6708/2008/12/039, arXiv:0808.3674.

[19] S. Schumann and F. Krauss, "A Parton shower algorithm based on Catani-Seymour dipole factorisation", *JHEP* **03** (2008) 038, doi:10.1088/1126-6708/2008/03/038, arXiv:0709.1027.

[20] T. Gleisberg et al., "Event generation with SHERPA 1.1", *JHEP* **02** (2009) 007, doi:10.1088/1126-6708/2009/02/007, arXiv:0811.4622.

[21] S. Hoeche, F. Krauss, S. Schumann, and F. Siegert, "QCD matrix elements and truncated showers", *JHEP* **05** (2009) 053, doi:10.1088/1126-6708/2009/05/053, arXiv:0903.1219.

[22] LHC Higgs Cross Section Working Group Collaboration, "Handbook of LHC Higgs Cross Sections: 1. Inclusive Observables", doi:10.5170/CERN-2011-002, arXiv:1101.0593.

[23] P. Nason and C. Oleari, "NLO Higgs boson production via vector-boson fusion matched with shower in POWHEG", *JHEP* **02** (2010) 037, doi:10.1007/JHEP02(2010)037, arXiv:0911.5299.

[24] E. Bagnaschi, G. Degrassi, P. Slavich, and A. Vicini, "Higgs production via gluon fusion in the POWHEG approach in the SM and in the MSSM", *JHEP* **02** (2012) 088, doi:10.1007/JHEP02(2012)088, arXiv:1111.2854.

[25] GEANT4 Collaboration, "GEANT4: a simulation toolkit", *Nucl. Instrum. Meth. A* **506** (2003) 250, doi:10.1016/S0168-9002(03)01368-8.

[26] N. Arkani-Hamed et al., "MARMOSET: The Path from LHC Data to the New Standard Model via On-Shell Effective Theories", (2007). arXiv:hep-ph/0703088.

[27] J. Alwall, P. C. Schuster, and N. Toro, "Simplified models for a first characterization of new physics at the LHC", *Phys. Rev. D* **79** (2009) 075020, doi:10.1103/PhysRevD.79.075020, arXiv:0810.3921.

[28] J. Alwall, M.-P. Le, M. Lisanti, and J. G. Wacker, "Model independent jets plus missing energy searches", *Phys. Rev. D* **79** (2009) 015005, doi:10.1103/PhysRevD.79.015005, arXiv:0809.3264.

[29] D. S. M. Alves, E. Izaguirre, and J. G. Wacker, "Where the sidewalk ends: jets and missing energy search strategies for the 7 TeV LHC", *JHEP* **10** (2011) 012, doi:10.1007/JHEP10(2011)012, arXiv:1102.5338.

[30] D. Alves et al., "Simplified models for LHC new physics searches", *J. Phys. G* **39** (2012) 105005, doi:10.1088/0954-3899/39/10/105005, arXiv:1105.2838.

[31] K. T. Matchev and S. D. Thomas, "Higgs and Z boson signatures of supersymmetry", *Phys. Rev. D* **62** (2000) 077702, doi:10.1103/PhysRevD.62.077702, arXiv:hep-ph/9908482.

[32] J. T. Ruderman and D. Shih, "General neutralino NLSPs at the early LHC", *JHEP* **08** (2012) 159, doi:10.1007/JHEP08(2012)159, arXiv:1103.6083.

[33] G. F. Giudice and R. Rattazzi, "Theories with gauge mediated supersymmetry breaking", *Phys. Rept.* **322** (1999) 419, doi:10.1016/S0370-1573(99)00042-3, arXiv:hep-ph/9801271.

[34] W. Beenakker et al., "Production of charginos, neutralinos and sleptons at hadron colliders", *Phys. Rev. Lett.* **83** (1999) 3780, doi:10.1103/PhysRevLett.83.3780, arXiv:hep-ph/9906298. [Erratum: doi:10.1103/PhysRevLett.100.029901].

[35] J. Alwall et al., "MadGraph5: going beyond", *JHEP* **06** (2011) 128, doi:10.1007/JHEP06(2011)128, arXiv:1106.0522.

[36] J. Alwall et al., "The automated computation of tree-level and next-to-leading order differential cross sections, and their matching to parton shower simulations", *JHEP* **07** (2014) 079, doi:10.1007/JHEP07(2014)079, arXiv:1405.0301.

[37] S. Höche et al., "Matching parton showers and matrix elements", (2006). arXiv:hep-ph/0602031.

[38] B. Fuks, M. Klasen, D. R. Lamprea, and M. Rothering, "Gaugino production in proton-proton collisions at a center-of-mass energy of 8 TeV", *JHEP* **10** (2012) 081, doi:10.1007/JHEP10(2012)081, arXiv:1207.2159.

[39] B. Fuks, M. Klasen, D. R. Lamprea, and M. Rothering, "Precision predictions for electroweak superpartner production at hadron colliders with Resummino", *Eur. Phys. J. C* **73** (2013) 2480, doi:10.1140/epjc/s10052-013-2480-0, arXiv:1304.0790.

[40] (CMS) Collaboration, "Searches for electroweak neutralino and chargino production in channels with Higgs, Z, and W bosons in pp collisions at 8 TeV", *Phys. Rev. D* **90** (Nov, 2014) 092007, doi:10.1103/PhysRevD.90.092007.

[41] CMS Collaboration, "Particle–flow event reconstruction in CMS and performance for jets, taus, and $E_{\mathrm{T}}^{\mathrm{miss}}$", CMS Physics Analysis Summary CMS-PAS-PFT-09-001, 2009.

[42] CMS Collaboration, "Commissioning of the particle-flow event reconstruction with the first LHC collisions recorded in the CMS detector", CMS Physics Analysis Summary CMS-PAS-PFT-10-011, 2010.

[43] M. Cacciari, G. P. Salam, and G. Soyez, "FastJet user manual", *Eur. Phys. J. C* **72** (2012) 1896, doi:10.1140/epjc/s10052-012-1896-2, arXiv:1111.6097.

[44] M. Cacciari, G. P. Salam, and G. Soyez, "The anti-$\mathrm{k_T}$ jet clustering algorithm", *JHEP* **04** (2008) 063, doi:10.1088/1126-6708/2008/04/063, arXiv:0802.1189.

[45] CMS Collaboration, "Missing transverse energy performance of the CMS detector", *JINST* **6** (2011) P09001, doi:10.1088/1748-0221/6/09/P09001, arXiv:1106.5048.

[46] CMS Collaboration, "Search for New Physics in the Multijet and Missing Transverse Momentum Final State in Proton-Proton Collisions at $\sqrt{s} = 7$ TeV", *Phys. Rev. Lett.* **109** (2012) 171803, doi:10.1103/PhysRevLett.109.171803, arXiv:1207.1898.

[47] CMS Collaboration, "Performance of the missing transverse energy reconstruction by the CMS experiment in $\sqrt{s}$ = 8 TeV pp data", CMS Physics Analysis Summary CMS-PAS-JME-13-003, 2013.

[48] CMS Collaboration, "Performance of b tagging at $\sqrt{s} = 8$ TeV in multijet, $\mathrm{t\bar{t}}$ and boosted topology events", CMS Physics Analysis Summary CMS-PAS-BTV-13-001, 2013.

[49] K. Arisaka et al., "Improved upper limit on the branching ratio B ($K_L^0 \to \mu^{\pm} e^{\pm}$)", *Phys. Rev. Lett.* **70** (1993) 1049, doi:10.1103/PhysRevLett.70.1049.

[50] J. Klein and A. Roodman, "Blind analysis in nuclear and particle physics", *Ann. Rev. Nucl. Part. Sci.* **55** (2005) 141, doi:10.1146/annurev.nucl.55.090704.151521.

[51] M. Kramer et al., "Supersymmetry production cross sections in pp collisions at $\sqrt{s} = 7$ TeV", arXiv:1206.2892.